Journal of Engineering Mathematics **26**: 21–37, 1992.
H.K. Kuiken and S.W. Rienstra (eds), Problems in Applied, Industrial and Engineering Mathematics.

Marangoni convection in V-shaped containers

H.W. HOOGSTRATEN
Department of Mathematics, University of Groningen, P.O. Box 800, 9700 AV Groningen, The Netherlands

and

H.C.J. HOEFSLOOT* and L.P.B.M. JANSSEN
Department of Chemical Engineering, University of Groningen, Groningen, The Netherlands

Abstract. This paper presents a numerical study of the time evolution of Marangoni convection in two V-shaped containers involved in the microgravity experiments reported in Hoefsloot et al. [7]. First the case of the triangular container with a plane gas/liquid interface is considered, next the container having the shape of a circular sector with a curved interface is dealt with. The numerical results show the same behaviour as observed experimentally: convection caused by macroscale effects in the former, and microconvection in the latter case.

1. Introduction

Marangoni convection, or surface tension driven convective flow, may occur when a solute evaporates from a liquid at a gas/liquid interface and the liquid's surface tension depends on the solute concentration. Perturbations of the mass transfer across the interface create local differences in surface tension, and the liquid at the interface will flow from locations with low surface tension towards locations with high surface tension. If this mechanism is sufficiently strong to overcome the counteracting viscous resistance, a convective flow is created in the liquid. In many cases a characteristic roll-cell pattern is seen to develop. Very often a second mechanism that can give rise to convective flow is present: buoyancy effects as a result of density variations (Rayleigh instability). In practice it is sometimes difficult to determine whether an observed convective flow is the result of Marangoni or Rayleigh instability, or of a combination of the two effects. We mention that both types of instability can also occur in the case of heat transfer across a gas/liquid interface, viz, when surface tension and/or density are temperature-dependent.

In chemical process industry Marangoni convection is considered to be an important phenomenon in mass transfer equipment, like packed-bed columns, where thin liquid films are in contact with a gas phase. It has been shown (see e.g. Nield [13]) that Marangoni instability determines the convective flows in thin liquid films, whereas Rayleigh instability is dominant in thick layers. Since the presence of roll-cell activity in a chemical reactor enhances mass transfer, thus leading to an improved performance, the study of the Marangoni effect is of practical importance.

Experimental work on Marangoni convection in thin liquid layers is somewhat problematic, because flow measurements in such layers are very difficult and in thick layers the simultaneous presence of Rayleigh convection is an obstacle. Therefore experiments are usually carried out in a microgravity environment, so that buoyancy effects are negligible and

*Present address: Department of Chemical Engineering, University of Amsterdam, Amsterdam, The Netherlands.

the restriction to thin liquid layers is removed. A number of years ago the Chemical Engineering Department of the University of Groningen (The Netherlands) started a program of microgravity experiments to study Marangoni convection. In all experiments the driving force for the convective flows was the evaporation of acetone into air from an acetone in water solution. For this liquid the surface tension is a decreasing function of the solute concentration. This function is usually taken to be a linear one for the range of concentration values under consideration. Marangoni convection near a plane gas/liquid interface was studied during the D1-Spacelab flight of 1985 (Lichtenbelt et al. [11], Dijkstra and Lichtenbelt [2]). Experiments concerning surface tension driven flow around a ventilated air bubble in the acetone in water solution, carried out during two sounding-rocket flights (1987, 1988) in Kiruna (Sweden) and during two parabolic-flight campaigns (1986, 1988) in Houston (USA), were meant to investigate the influence of interface curvature (Dijkstra and Lichtenbelt [2], Lichtenbelt [10], Hoefsloot and Janssen [3, 4], Hoefsloot et al. [9]). The latest experiments were performed in 1990 with narrow V-shaped containers on board of the Caravelle 234 airplane at the Centre d'Essais en Vols in Bretigny (France), see Hoefsloot et al. [7].

The experiments showed that it makes sense to distinguish between two types of Marangoni convection: convection created by overall surface tension gradients occurring initially in the system (macroscale convection or, shortly, macroconvection) and convection which is the result of hydrodynamic instability (microscale convection or microconvection). We emphasize that this difference concerns only the mechanism governing the *onset* of the convective flow, and not necessarily the final flow development towards a more or less regular roll-cell pattern. Macroscale effects are mostly due to geometrical factors which lead to inhomogeneous mass transfer across the interface, whereas microconvection occurs when evaporation is uniform. A linear stability analysis describing theoretically the initial stage of microscale convection has been presented by Hoefsloot et al. for a cylindrically curved interface [5] and for the spherical interface separating a ventilated air bubble from the surrounding liquid [6, 8]. For the latter system numerical results describing the longer-time evolution of Marangoni convection are reported in Hoefsloot et al. [9].

In this paper we present a numerical study of the time evolution of Marangoni convection in two of the V-shaped containers involved in the experiments described in [7]. The flows in this type of container are believed to be representative for those occurring in dead zones (stagnant liquid zones) in packings in mass transfer equipment. Two different containers will be considered: a triangular one with a plane gas/liquid interface, in which convective flow due to macroscale effects is to be expected, and another having the shape of a circular sector with a curved interface, which will show microscale convection. In Section 2 the experimental setup and results concerning these two containers are briefly outlined. The mathematical formulation of the two-dimensional coupled fluid-flow/mass-diffusion problem is given in Section 3, together with a discussion of the numerical solution technique. In Section 4 the numerical results are presented, and the paper ends with Section 5 in which some concluding remarks are made.

2. Results of microgravity experiments

The experimental setup as well as the experimental results are fully described in Hoefsloot et al. [7]. For completeness a brief summary will be given here. The experiments were

performed during a number of parabolic flights, in each of which a microgravity level of less than $0.05g$ was attained for a period of about 17 seconds. The main parts of the setup were narrow V-shaped glass containers, filled with a 5 wt% acetone solution in water in which, due to the evaporation of the acetone, Marangoni convection will start. The liquid contained tracer particles which were monitored by both a video and a photo camera. Figure 1 presents two photographs that are representative for the whole experiment. The triangular container with the flat gas/liquid interface shows two large roll cells (Fig. 1a). In the container with the curved interface (Fig. 1b), a number of smaller roll cells are visible near the interface,

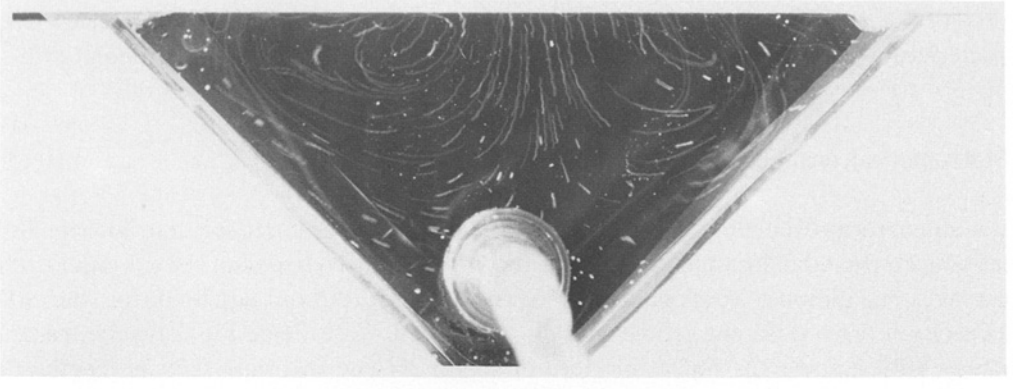

(a)

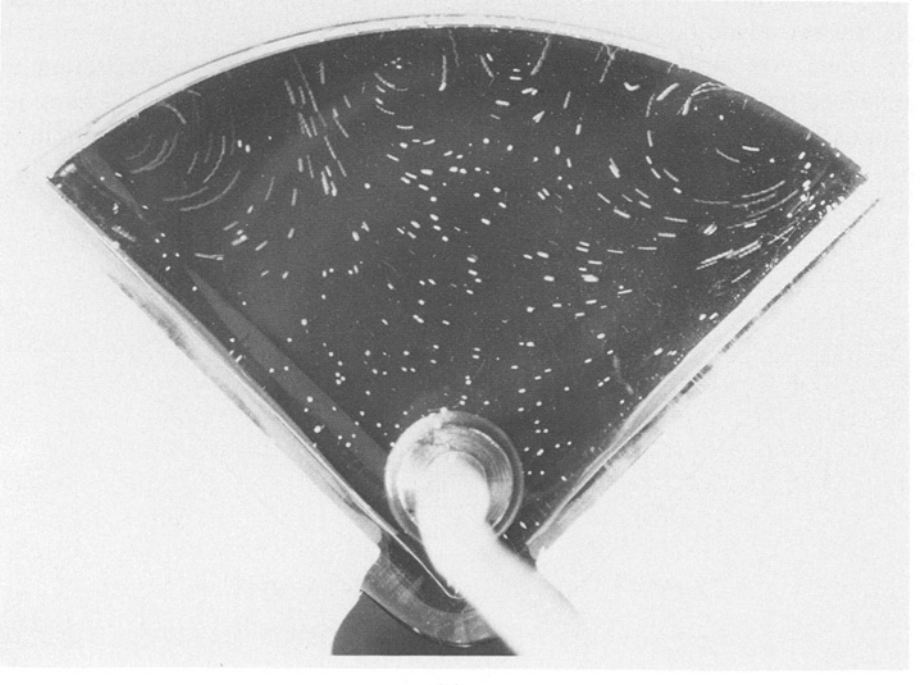

(b)

Fig. 1. Roll cells observed in a triangular container with plane interface (a) and a container with curved interface (b). The largest dimension of both containers is 28.3 mm. Camera shutter time: 1 s. Photograph (a) was taken 7.4 s after injection of the liquid into the container, (b) after 9.3 s.

whereas the liquid bulk remains more or less quiescent. The maximum flow velocities were about 4 mm/s in the former case, and about 1.5 mm/s in the latter.

The difference between these two flows has already been explained by Hoefsloot et al. [7]. The geometry of the triangular container leads to a depletion of acetone in the corner regions, creating a surface tension gradient which forces the liquid at the interface to flow towards the corners (macroscale effect). For the container with the curved interface the mass transfer by evaporation across the interface is homogeneous, and the onset of the convective flow is entirely due to hydrodynamic instability (microscale convection). This type of instability often tends to create a large number of small roll cells at the initial stage, with various coalescences or breakups of cells at later times, contrary to the rather stable two-cell pattern of the macroscale case. Apart from this, the flow caused by the macroscale effect is characterized by much larger flow velocities than in the case of microconvection.

3. Mathematical formulation and numerical solution method

The mathematical modelling of the convective flows will be based on the Navier–Stokes equations for two-dimensional flow of an incompressible Newtonian viscous liquid under zero-gravity conditions, combined with a convection/diffusion equation for the solute concentration. Two different geometries are considered. Case I (see Fig. 2) is the triangular container with a plane gas/liquid interface of length $2H$ and two rigid sides of length $H\sqrt{2}$. This case corresponds to the experimental container depicted in Fig. 1a. Case II (see Fig. 3) corresponds to the experiment shown in Fig. 1b. The liquid region has the shape of a sector of a circle with radius H and opening angle $\pi/2$. The circular boundary is the gas/liquid interface, the two plane boundaries are rigid walls.

Length, time, velocity, stream function, vorticity and solute concentration are non-dimensionalized by scaling with respectively, H, H^2/ν, ν/H, ν, ν/H^2 and c_{in}. Here ν denotes the kinematic liquid viscosity and c_{in} is the (uniform) initial solute concentration.

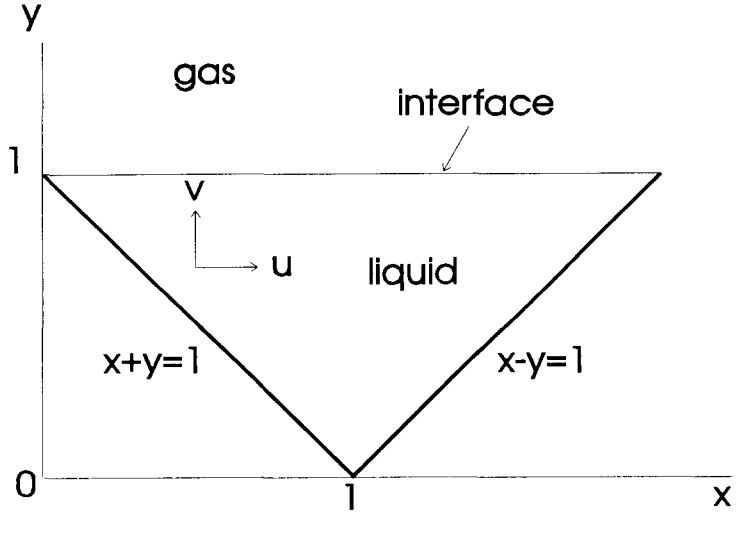

Fig. 2. The triangular container with plane gas/liquid interface in the dimensionless x, y-plane (case I).

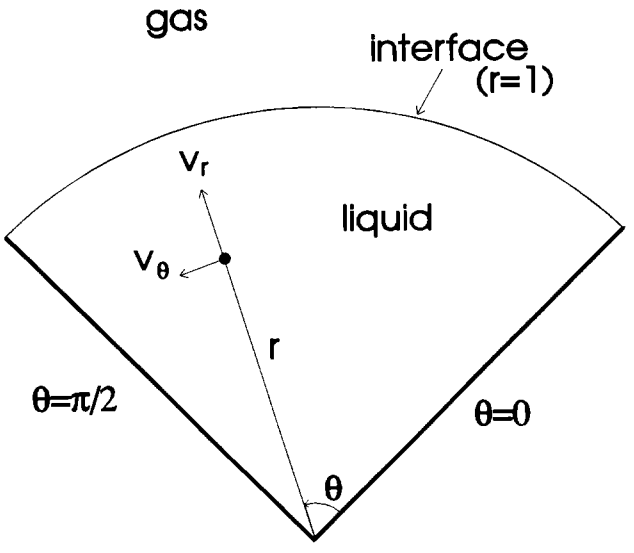

Fig. 3. The circular-sector container with curved gas/liquid interface in the dimensionless r, θ-plane (case II).

3.1. Case I (plane interface)

In the non-dimensional formulation the liquid region in the x, y-plane is given by $x + y > 1$, $x - y < 1$, $y < 1$ (see Fig. 2). After introduction of the stream function Ψ and the vorticity ω by the relations

$$u = -\frac{\partial \Psi}{\partial y}, \qquad v = \frac{\partial \Psi}{\partial x}, \qquad \omega = \frac{\partial u}{\partial y} - \frac{\partial v}{\partial x},$$

where (u, v) is the velocity vector, the governing equations for Ψ, ω and solute concentration c can be written as

$$\frac{\partial \omega}{\partial t} - \frac{\partial \Psi}{\partial y}\frac{\partial \omega}{\partial x} + \frac{\partial \Psi}{\partial x}\frac{\partial \omega}{\partial y} = \nabla^2 \omega, \tag{1}$$

$$\omega = -\nabla^2 \Psi, \tag{2}$$

$$\frac{\partial c}{\partial t} - \frac{\partial \Psi}{\partial y}\frac{\partial c}{\partial x} + \frac{\partial \Psi}{\partial x}\frac{\partial c}{\partial y} = \frac{1}{\mathrm{Sc}}\nabla^2 c, \tag{3}$$

where t is the time variable, ∇^2 is the two-dimensional Laplacian $\partial^2/\partial x^2 + \partial^2/\partial y^2$ and Sc denotes the Schmidt number $\nu/\mathbb{D}$ with $\mathbb{D}$ the coefficient of mass diffusion in the liquid.

At the solid walls we have the boundary conditions

$$\Psi = \frac{\partial \Psi}{\partial x} + \frac{\partial \Psi}{\partial y} = \frac{\partial c}{\partial x} + \frac{\partial c}{\partial y} = 0, \quad \text{for } x + y = 1,$$

$$\Psi = \frac{\partial \Psi}{\partial x} - \frac{\partial \Psi}{\partial y} = \frac{\partial c}{\partial x} - \frac{\partial c}{\partial y} = 0, \quad \text{for } x - y = 1,$$

implying zero flow velocity (no-slip condition) and mass impermeability. Assuming that the gas/liquid interface does not deform, we may put

$$\Psi = 0 \quad \text{at} \quad y = 1 .$$

Further we impose the mass transfer condition

$$\frac{\partial c}{\partial y} + \mathrm{Bi}\, c = 0 \quad \text{at} \quad y = 1 ,$$

where Bi denotes the Biot number defined as $kH/\mathbb{D}$ with k the mass transfer coefficient of the gas phase. The tangential stress balance at the interface gives (see Dijkstra and Van de Vooren [1])

$$\omega\left(= -\frac{\partial u}{\partial y}\right) = \frac{\mathrm{Ma}}{\mathrm{Sc}} \frac{\partial c}{\partial x} \quad \text{at} \quad y = 1 ,$$

where Ma is the Marangoni number

$$\mathrm{Ma} = -\frac{(\mathrm{d}\gamma/\mathrm{d}\tilde{c})c_{\mathrm{in}}H}{\mu\mathbb{D}} .$$

The derivative $\mathrm{d}\gamma/\mathrm{d}\tilde{c}$ of the (dimensional) surface tension γ with respect to the dimensional solute concentration $\tilde{c}$ is assumed to be equal to a negative constant.

Finally, we have the initial conditions

$$\Psi = \omega = 0 , \qquad c = 1 \quad \text{for } t = 0 .$$

The above initial/boundary-value problem has been solved numerically by the well-known Alternating Direction Implicit (ADI) finite difference method (see e.g. [12] and [14]). The discretization for this method leads, after linearization, to sets of linear algebraic equations with a tridiagonal coefficient matrix which are relatively easy to solve. The time-discretized form of equations (1)–(3) reads

$$\frac{\omega^{m+1/2} - \omega^m}{\Delta t} = \frac{1}{2}\left(\frac{\partial^2 \omega^{m+1/2}}{\partial y^2} - \frac{\partial \Psi^m}{\partial x}\frac{\partial \omega^{m+1/2}}{\partial y}\right) + \frac{1}{2}\left(\frac{\partial^2 \omega^m}{\partial x^2} + \frac{\partial \Psi^m}{\partial y}\frac{\partial \omega^m}{\partial x}\right), \tag{4}$$

$$\frac{\omega^{m+1} - \omega^{m+1/2}}{\Delta t} = \frac{1}{2}\left(\frac{\partial^2 \omega^{m+1/2}}{\partial y^2} - \frac{\partial \Psi^m}{\partial x}\frac{\partial \omega^{m+1/2}}{\partial y}\right) + \frac{1}{2}\left(\frac{\partial^2 \omega^{m+1}}{\partial x^2} + \frac{\partial \Psi^m}{\partial y}\frac{\partial \omega^{m+1}}{\partial x}\right), \tag{5}$$

$$\frac{\Psi^{n+1/2} - \Psi^n}{\tau} = \frac{1}{2}\left(\frac{\partial^2 \Psi^{n+1/2}}{\partial y^2} + \frac{\partial^2 \Psi^n}{\partial x^2} + \omega^{m+1}\right), \tag{6}$$

$$\frac{\Psi^{n+1} - \Psi^{n+1/2}}{\tau} = \frac{1}{2}\left(\frac{\partial^2 \Psi^{n+1/2}}{\partial y^2} + \frac{\partial^2 \Psi^{n+1}}{\partial x^2} + \omega^{m+1}\right), \tag{7}$$

$$\frac{c^{m+1/2} - c^m}{\Delta t} = \frac{1}{2}\left(\frac{1}{\mathrm{Sc}}\frac{\partial^2 c^{m+1/2}}{\partial y^2} - \frac{\partial \Psi^{m+1}}{\partial x}\frac{\partial c^{m+1/2}}{\partial y}\right) + \frac{1}{2}\left(\frac{1}{\mathrm{Sc}}\frac{\partial^2 c^m}{\partial x^2} + \frac{\partial \Psi^{m+1}}{\partial y}\frac{\partial c^m}{\partial x}\right), \tag{8}$$

$$\frac{c^{m+1}-c^{m+1/2}}{\Delta t}=\frac{1}{2}\left(\frac{1}{\mathrm{Sc}}\frac{\partial^2 c^{m+1/2}}{\partial y^2}-\frac{\partial \Psi^{m+1}}{\partial x}\frac{\partial c^{m+1/2}}{\partial y}\right)+\frac{1}{2}\left(\frac{1}{\mathrm{Sc}}\frac{\partial^2 c^{m+1}}{\partial x^2}+\frac{\partial \Psi^{m+1}}{\partial y}\frac{\partial c^{m+1}}{\partial x}\right), \tag{9}$$

where the superscript m denotes the time level $t=m\,\Delta t$. In equations (6) and (7) a pseudo-time discretization has been introduced with time step τ and counter n. All derivatives with respect to the spatial variables x and y occurring both in the equations and in the boundary conditions have been replaced by second-order difference quotients.

A nonuniform rectangular grid has been used. The grid lines parallel to the x-axis are given by

$$y=y_i=-0.99\,(i/N)^2+1.99(i/N)\,,\quad i=0,1,\ldots,N\,.$$

The grid lines $x=$ constant run through the points of intersection of the lines $y=y_i$ with the boundaries $x\pm y=1$. In this way we have the highest density of grid points in the region near the interface where the largest velocity and concentration gradients will occur.

The numerical computation is carried out as follows. Assuming that Ψ, ω and c are known at time level m, first the value $\omega^{m+1/2}$ at the intermediate level $m+1/2$ is computed from (4) and using this value of $\omega^{m+1/2}$ in (5), the value of ω^{m+1} is computed. Next, Ψ at level $m+1$ is computed iteratively from (6) and (7) with n as iteration counter and using the stop criterion $|\Psi^n-\Psi^{n+1}|<10^{-6}$. During this iteration, the pseudo-time step τ is not kept fixed, but it can be enlarged when n increases, thus saving computer time. Finally, the computed value Ψ^{m+1} is used in (8) and (9) to compute subsequently the concentration values $c^{m+1/2}$ and c^{m+1}. At this stage Ψ, ω and c are known at time level $m+1$, so m can now be changed into $m+1$ and the procedure is repeated. This method is probably not the most cost-efficient one, but it is reliable and works well also for large values of Ma and Sc.

3.2. *Case II (curved interface)*

In this case we use polar coordinates r and θ in terms of which the liquid region is given by $0<r<1$, $0<\theta<\pi/2$ (see Fig. 3). The velocity components v_r and v_θ are now related to Ψ and ω in the following way:

$$v_\theta=\frac{\partial \Psi}{\partial r}\,,\qquad v_r=-\frac{1}{r}\frac{\partial \Psi}{\partial \theta}\,,\qquad \omega=-\frac{1}{r}\frac{\partial v_r}{\partial \theta}+\frac{1}{r}\frac{\partial (v_\theta r)}{\partial r}\,,$$

and the equations to be solved for Ψ, ω and c read

$$\frac{\partial \omega}{\partial t}=\frac{\partial^2 \omega}{\partial r^2}+\frac{1}{r^2}\frac{\partial^2 \omega}{\partial \theta^2}+\frac{1}{r}\frac{\partial \omega}{\partial r}-\frac{1}{r}\left[\frac{\partial \Psi}{\partial r}\frac{\partial \omega}{\partial \theta}-\frac{\partial \Psi}{\partial \theta}\frac{\partial \omega}{\partial r}\right], \tag{10}$$

$$\omega=\frac{\partial^2 \Psi}{\partial r^2}+\frac{1}{r^2}\frac{\partial^2 \Psi}{\partial \theta^2}+\frac{1}{r}\frac{\partial \Psi}{\partial r}\,, \tag{11}$$

$$\frac{\partial c}{\partial t}=\frac{1}{\mathrm{Sc}}\left[\frac{\partial^2 c}{\partial r^2}+\frac{1}{r^2}\frac{\partial^2 c}{\partial \theta^2}+\frac{1}{r}\frac{\partial c}{\partial r}\right]+\frac{1}{r}\left(\frac{\partial \Psi}{\partial \theta}\frac{\partial c}{\partial r}-\frac{\partial \Psi}{\partial r}\frac{\partial c}{\partial \theta}\right). \tag{12}$$

The boundary conditions at the solid walls are

$$\Psi = \frac{\partial c}{\partial \theta} = 0\,, \qquad \omega = \frac{\partial^2 \Psi}{\partial^2 r}\,, \quad \text{at } \theta = 0 \text{ and } \theta = \pi/2\,.$$

Analogous to the preceding case, we impose three boundary conditions at the gas/liquid interface $r = 1$:

$$\Psi = 0\,, \qquad \frac{\partial c}{\partial r} = -\mathrm{Bi}\, c \quad \text{at} \quad r = 1\,,$$

and

$$\omega - 2\,\frac{\partial \Psi}{\partial r}\left(= \frac{\partial v_\theta}{\partial r} - \frac{v_\theta}{r}\right) = -\frac{\mathrm{Ma}}{\mathrm{Sc}}\,\frac{1}{r}\,\frac{\partial c}{\partial \theta} \quad \text{at} \quad r = 1\,.$$

The initial conditions at $t = 0$ are:

$$\omega = 0\,, \qquad \Psi = 0 \quad \text{and} \quad c = 1\,.$$

Since the above initial/boundary value problem possesses the motionless solution $\Psi = \omega = 0$, $c = c_0(r, t)$, a very small initial perturbation of the interfacial value of c will be introduced to trigger off numerically the onset of micro-scale convection.

As in case I, the numerical solution of the above problem has been obtained by means of an ADI method. The time-discretized version of equations (10)–(12) is

$$\frac{\omega^{m+1/2} - \omega^m}{\Delta t} = \frac{1}{2}\left(\frac{1}{r^2}\,\frac{\partial^2 \omega^{m+1/2}}{\partial \theta^2} - \frac{1}{r}\,\frac{\partial \Psi^m}{\partial r}\,\frac{\partial \omega^{m+1/2}}{\partial \theta}\right) + \frac{1}{2}\left(\frac{\partial^2 \omega^m}{\partial r^2} + \frac{1}{r}\left(1 + \frac{\partial \Psi^m}{\partial \theta}\right)\frac{\partial \omega^m}{\partial r}\right), \tag{13}$$

$$\frac{\omega^{m+1} - \omega^{m+1/2}}{\Delta t} = \frac{1}{2}\left(\frac{1}{r^2}\,\frac{\partial^2 \omega^{m+1/2}}{\partial \theta^2} - \frac{1}{r}\,\frac{\partial \Psi^m}{\partial r}\,\frac{\partial \omega^{m+1/2}}{\partial \theta}\right) + \frac{1}{2}\left(\frac{\partial^2 \omega^{m+1}}{\partial r^2} + \frac{1}{r}\left(1 + \frac{\partial \Psi^m}{\partial \theta}\right)\frac{\partial \omega^{m+1}}{\partial r}\right), \tag{14}$$

$$\frac{\Psi^{n+1/2} - \Psi^n}{\tau} = \frac{1}{2}\left(\frac{1}{r^2}\,\frac{\partial^2 \Psi^{n+1/2}}{\partial \theta^2} + \frac{\partial^2 \Psi^n}{\partial r^2} + \frac{1}{r}\,\frac{\partial \Psi^n}{\partial r} - \omega^{m+1}\right), \tag{15}$$

$$\frac{\Psi^{n+1} - \Psi^{n+1/2}}{\tau} = \frac{1}{2}\left(\frac{1}{r^2}\,\frac{\partial^2 \Psi^{n+1/2}}{\partial \theta^2} + \frac{\partial^2 \Psi^{n+1}}{\partial r^2} + \frac{1}{r}\,\frac{\partial \Psi^{n+1}}{\partial r} - \omega^{m+1}\right), \tag{16}$$

$$\frac{c^{m+1/2} - c^m}{\Delta t} = \frac{1}{2}\left(\frac{1}{\mathrm{Sc}}\,\frac{1}{r^2}\,\frac{\partial^2 c^{m+1/2}}{\partial \theta^2} - \frac{\partial \Psi^{m+1}}{\partial r}\,\frac{1}{r}\,\frac{\partial c^{m+1/2}}{\partial \theta}\right) + \frac{1}{2}\left(\frac{1}{\mathrm{Sc}}\left[\frac{\partial^2 c^m}{\partial r^2} + \frac{1}{r}\,\frac{\partial c^m}{\partial r}\right] + \frac{1}{r}\,\frac{\partial \Psi^{m+1}}{\partial \theta}\,\frac{\partial c^m}{\partial r}\right), \tag{17}$$

$$\frac{c^{m+1} - c^{m+1/2}}{\Delta t} = \frac{1}{2}\left(\frac{1}{\mathrm{Sc}}\,\frac{1}{r^2}\,\frac{\partial^2 c^{m+1/2}}{\partial \theta^2} - \frac{\partial \Psi^{m+1}}{\partial r}\,\frac{1}{r}\,\frac{\partial c^{m+1/2}}{\partial \theta}\right) + \frac{1}{2}\left(\frac{1}{\mathrm{Sc}}\left[\frac{\partial^2 c^{m+1}}{\partial r^2} + \frac{1}{r}\,\frac{\partial c^{m+1}}{\partial r}\right] + \frac{1}{r}\,\frac{\partial \Psi^{m+1}}{\partial \theta}\,\frac{\partial c^{m+1}}{\partial r}\right), \tag{18}$$

where the superscript m denotes the time level $t = m\,\Delta t$. As in the discretized equations for

case I, τ denotes the pseudo-time step and n the pseudo-time level. All derivatives with respect to the spatial variables r and θ occurring in the basic equations and in the boundary conditions have been replaced by second-order differences. An equidistant grid has been used in the θ-direction, whereas in the r-direction a non-uniform grid has been used with a higher density of grid points near the interface $r = a/H$ where the concentration and velocity gradients are large. The non-equidistant grid points have been defined as:

$$r_i = -0.9(i/N)^2 + 1.9(i/N), \quad i = 0, 1, \ldots, N.$$

The numerical computation is carried out in the same way as in case I.

3.3. *Accuracy and convergence of the numerical method*

The ADI method which has been applied to solve the problems numerically has a first-order convergence rate in the time variable and second-order convergence with respect to the spatial variables. To check the correctness of the numerical algorithms a number of tests has been carried out. Since the convergence behaviour for case II is somewhat more intricate than for case I, we begin with some tests concerning case II.

Table 1 shows values of the maximum of the stream function (Ψ_{max}) and the velocity at the interface at $\theta = 22.5°$ (denoted by $V_{22.5}$) at the point of time $t = 1.25 \times 10^{-3}$ for the parameter values $Ma = 10^5$, $Sc = 100$ and $Bi = 55-100(\theta/\pi)$. Note that Bi has been chosen here as a function of θ along the interface, so that an artificial macroscale effect has been introduced and therefore no initial disturbance is required to start the convection. The computation has been done for three $\theta \times r$ grids (41×41, 81×81 and 161×161 points) and three Δt values (5×10^{-5}, 2.5×10^{-5} and 1.25×10^{-5}). The values of Ψ_{max} and $V_{22.5}$ show the expected convergence behaviour.

In the next test for case II the Biot number has been taken constant ($Bi = 20$) and there is an initial perturbed interfacial concentration given by

$$c = \begin{cases} 0.999 + 0.001(j/m), & j = 0, \ldots, M, \\ 1.001 - 0.001(j/M), & j = M, \ldots, 2M, \end{cases}$$

where $2M + 1$ is the number of grid points in θ-direction and j runs from $j = 0$ (corresponding to $\theta = 0$) to $j = 2M$ ($\theta = \pi/2$). To make this disturbance compatible with respect to the three spatial grids which have been used in this test, the first row below the interface in the 81×81 grid is given the linearly interpolated value between the undisturbed value ($c = 1$) of the second row and the interfacial value of c. For the 161×161 grid this interpolation is done for three rows, and for the 321×321 grid for seven rows. The computations were performed with $Ma = 10^5$, $Sc = 100$ and $\Delta t = 1.25 \times 10^{-5}$. The results for Ψ_{max} and $V_{22.5}$ at time $t = 2.5 \times 10^{-4}$, given in Table 2, demonstrate the desired convergence behaviour.

Table 1. Test results for case II: θ-dependent Biot number, no initial concentration perturbation.

grid	41×41		81×81		161×161	
Δt	Ψ_{max}	$V_{22.5}$	Ψ_{max}	$V_{22.5}$	Ψ_{max}	$V_{22.5}$
5×10^{-5}	0.0987	−3.768	0.0849	−3.397	0.0817	−3.314
2.5×10^{-5}	0.1013	−3.832	0.0874	−3.464	0.0842	−3.384
1.25×10^{-5}	0.1027	−3.864	0.0886	−3.497	0.0854	−3.416

Table 2. Test results for case II: constant Biot number, perturbed initial concentration (see text).

grid	81×81		161×161		321×321	
t	Ψ_{max}	$V_{22.5}$	Ψ_{max}	$V_{22.5}$	Ψ_{max}	$V_{22.5}$
2.5×10^{-4}	2.12×10^{-4}	−0.00631	2.52×10^{-4}	−0.00751	2.61×10^{-4}	−0.00776

A further computation, making use of an 81×161 grid and keeping the remaining parameter settings unchanged, gave a value for $V_{22.5}$ that differed only 2×10^{-7} from the 161×161 value of Table 2. Changing the time step to $\Delta t = 2.5 \times 10^{-5}$ and keeping all other settings the same gave $\Psi_{max} = 2.59 \times 10^{-4}$ on the 161×161 grid.

The above tests show that the convergence behaviour is as expected and accuracy is good for small time. To see how the accuracy is for larger values of t, computations have been carried out for case II on two $\theta \times r$ grids (161×321 and 321×641 points) with $\Delta t = 2.5 \times 10^{-5}$, $\mathrm{Ma} = 10^5$ and $\mathrm{Sc} = 100$ and $\mathrm{Bi} = 20$. The initial perturbed concentration along the interface is the same as above, with linearly interpolated c-values for the first three rows below the interface for the coarser grid, and for the first seven rows in the case of the finest grid. The results for Ψ_{max} are given in Table 3, from which it can be observed that accuracy deteriorates gradually in time, but it remains acceptable for $t \leq 7.5 \times 10^{-3}$.

For case I, being less difficult than case II, only one test is presented here with the parameter values $\mathrm{Ma} = 10^5$, $\mathrm{Sc} = 100$ and $\mathrm{Bi} = 20$. Three spatial ($x \times y$) grids were used with time step $\Delta t = 2.5 \times 10^{-5}$. Table 4 gives results for Ψ_{max}. From this table it can be seen that accuracy is reasonable as long as t is smaller than 1.25×10^{-2}.

3.4. Choice of parameters

In the numerical computations of which the results will be presented in the next section, the following parameter values have been used: $\mathrm{Ma} = 10^5$, $\mathrm{Sc} = 100$ and $\mathrm{Bi} = 20$. Theoretically, the Marangoni number would be about 10^8, but under experimental circumstances the value will mostly be several orders of magnitude smaller. The choice of $\mathrm{Sc} = 100$ instead of the actual value of acetone in water (which is 787), is a compromise. With the real value of Sc unacceptably small time steps would have been required to suppress numerical instabilities in

Table 3. Test results for case II: constant Biot number, perturbed initial concentration (see text).

grid	161×321	321×641
t	Ψ_{max}	Ψ_{max}
6.25×10^{-4}	0.00039	0.00041
1.25×10^{-3}	0.00053	0.00057
2.5×10^{-3}	0.00070	0.00076
5.0×10^{-3}	0.00087	0.00094
7.5×10^{-3}	0.00096	0.00104
1.0×10^{-2}	0.00103	0.00177
1.25×10^{-2}	0.00249	0.00397

Table 4. Test results for case I: constant Biot number, no initial concentration perturbation.

grid	161 × 81	321 × 161	641 × 321
t	Ψ_{max}	Ψ_{max}	Ψ_{max}
6.25×10^{-4}	0.0011	0.0007	0.0006
1.25×10^{-3}	0.0043	0.0030	0.0025
2.5×10^{-3}	0.0140	0.0109	0.0095
5.0×10^{-3}	0.0345	0.0265	0.0237
7.5×10^{-3}	0.0483	0.0418	0.0415
1.0×10^{-2}	0.2020	0.2180	0.2059
1.25×10^{-2}	0.5381	0.5323	0.4609

the solution (like wiggles). Lowering Sc increases the weight of the diffusive terms with respect to the convective terms, thus improving numerical stability. The chosen value of Bi is in the usual range of experimental values.

The spatial grid used for case I was the $x \times y$ grid of 641×321 points given in Table 4, and for case II the $\theta \times r$ grid of 321×641 points given in Table 3 was used. In all computations Δt was equal to 2.5×10^{-5}.

4. Numerical results

The numerical results are presented in the form of contour plots of the stream function Ψ for various points in time. Figure 4 shows some results for case I at times $t = t_1 = 2.5 \times 10^{-3}$, $2t_1$, $3t_1$, $4t_1$ and $5t_1$. The corresponding values of Ψ_{max} can be found in Table 4. It is seen that the characteristic roll-cell pattern for this macroscale case emerges: a quite stable pattern of two large roll cells, in accordance with the experimental observations. At $t = 3t_1$, an additional small cell is seen in each corner region, but it vanishes again soon afterwards. Although the plot for $t = 5t_1$ is not to be completely trusted from a numerical point of view (see Table 4), it has nevertheless been included since it confirms the global impression of a stable two-cell pattern for case I.

The first set of results for case II is represented by Fig. 5. The slightly perturbed initial concentration distribution, which is symmetric with respect to the line $\theta = \pi/4$, is the same as the one used in the second and third numerical test for case II (see previous section). This initial concentration has been chosen because the initial flow pattern consists of two large roll cells and resembles the flow pattern created by the injection of the liquid into the container during the experiment. The points in time for which the plots have been made correspond to those of Table 3: $t = t_1 = 2.5 \times 10^{-3}$, $2t_1$, $3t_1$ and $4t_1$. The initial two-cell pattern is clearly not persistent: the first stage of breakup into smaller cells is seen to occur in Figs 5c,d. This tendency towards a pattern of many small cells near the interface, along with a nearly motionless liquid bulk, is typical of microconvection. Comparing the values of Ψ_{max} for this case (see Table 3) with those for case I (see Table 4), it is clear that the macroscale effects of case I lead to higher liquid flow velocities than the microscale effects of case II.

Figures 6 and 7 show two simulations with initial disturbances leading to a flow pattern with a relatively large number of roll cells. In the case of Fig. 6 the initial concentration has

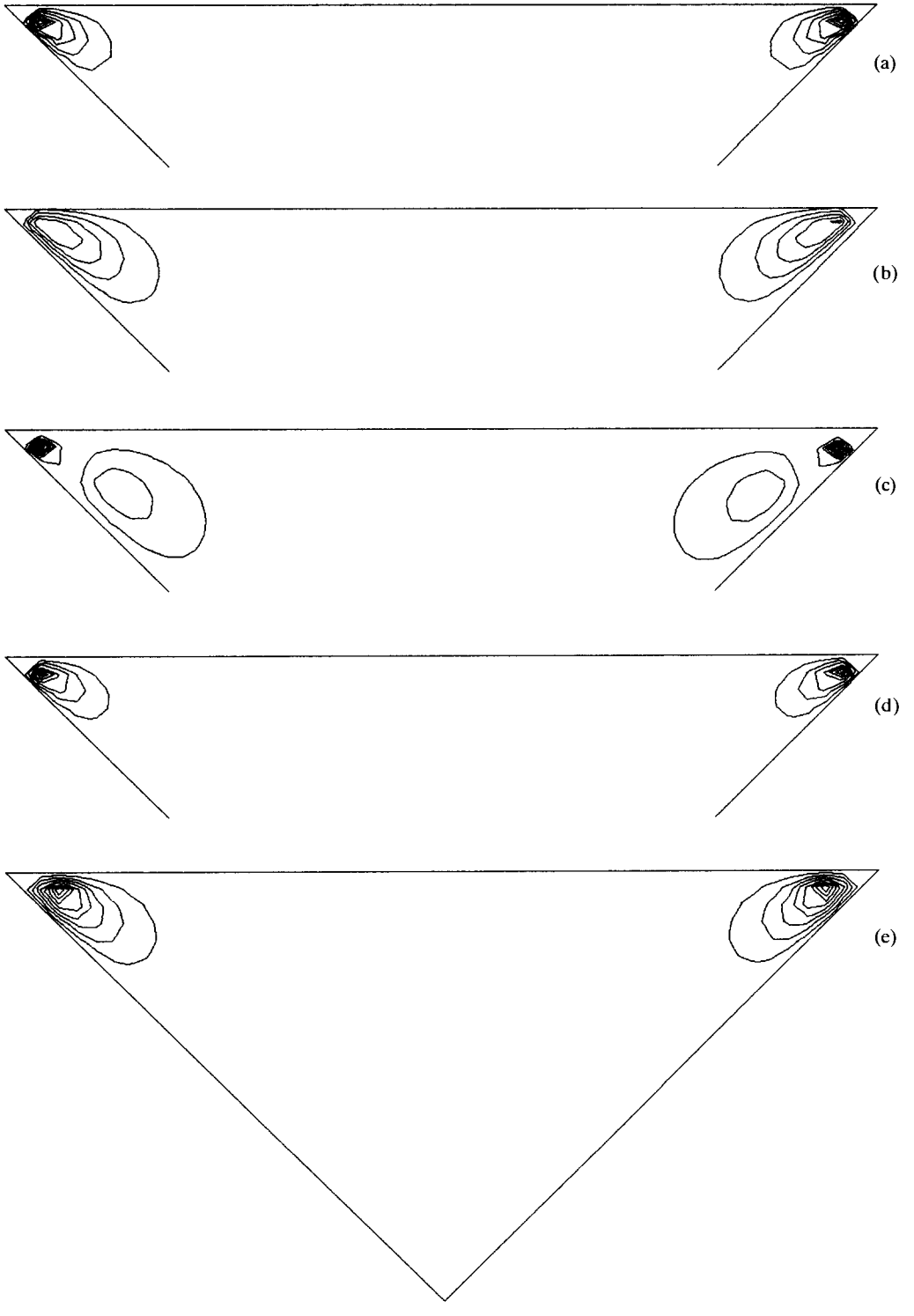

Fig. 4. Contour plots of the stream function for case I at dimensionless times t_1 (a), $2t_1$ (b), $3t_1$ (c), $4t_1$ (d) and $5t_1$ (e), where $t_1 = 2.5 \times 10^{-3}$.

been perturbed by assigning the value $c = 0.999$ to the five grid points $j = 0$, 80, 160, 240 and 320 on the interface, whereas in Fig. 7 this has been done for the eleven grid points $j = 0, 32, \ldots, 288, 320$. Although the time evolution of the patterns is slow in both cases (which, of course, is a typical property of microconvection), a tendency towards an increase of the number of cells is visible. These microconvection simulations would require extremely large computing times to monitor their full evolution in time. For each set of results presented above the computing time amounted to several hours on a Cyber 962 mainframe.

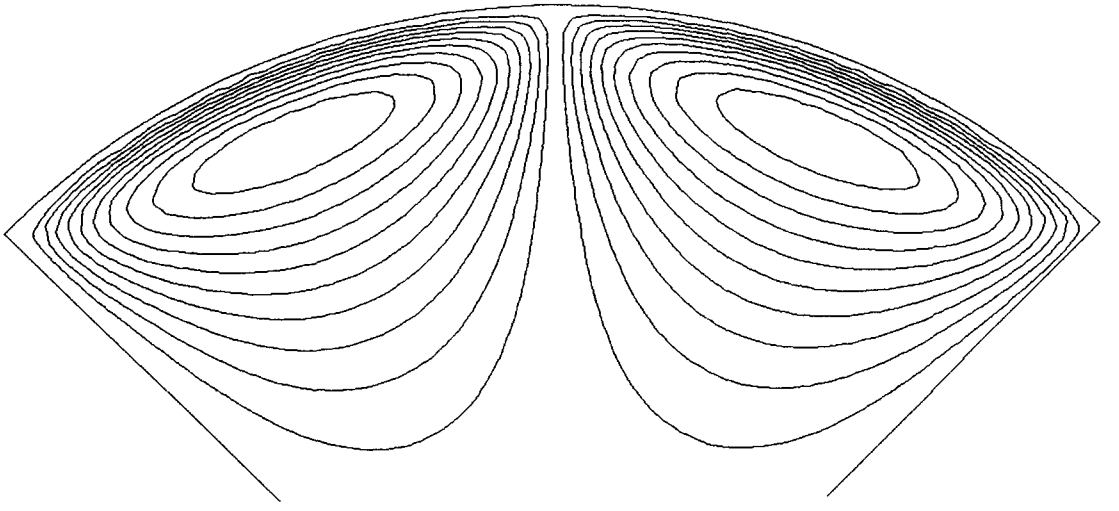

(a)

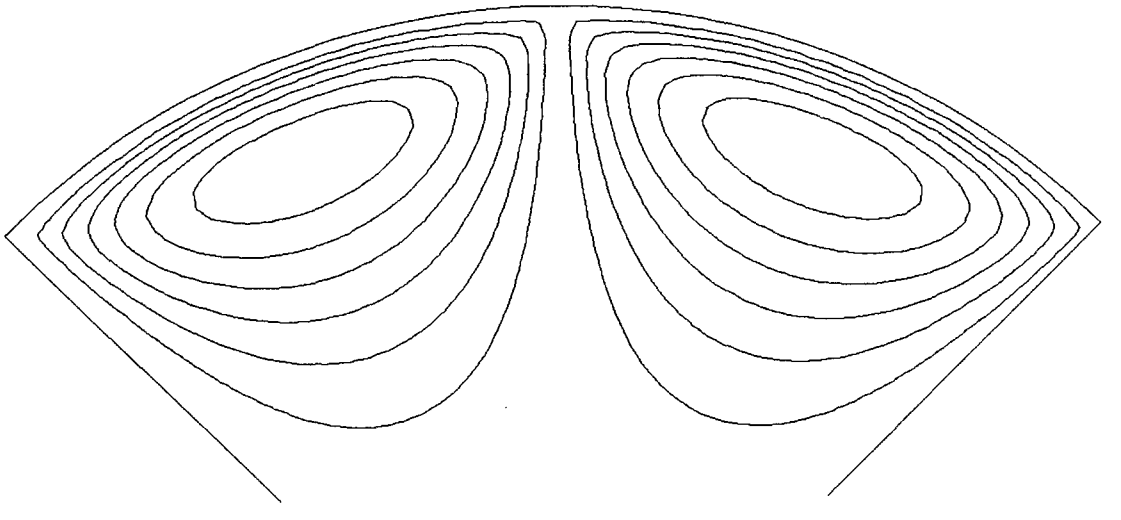

(b)

Fig. 5. Contour plots of the stream function for case II at dimensionless times t_1 (a), $2t_1$ (b), $3t_1$ (c) and $4t_1$ (d), where $t_1 = 2.5 \times 10^{-3}$, computed from the symmetrically perturbed initial concentration distribution described in the text.

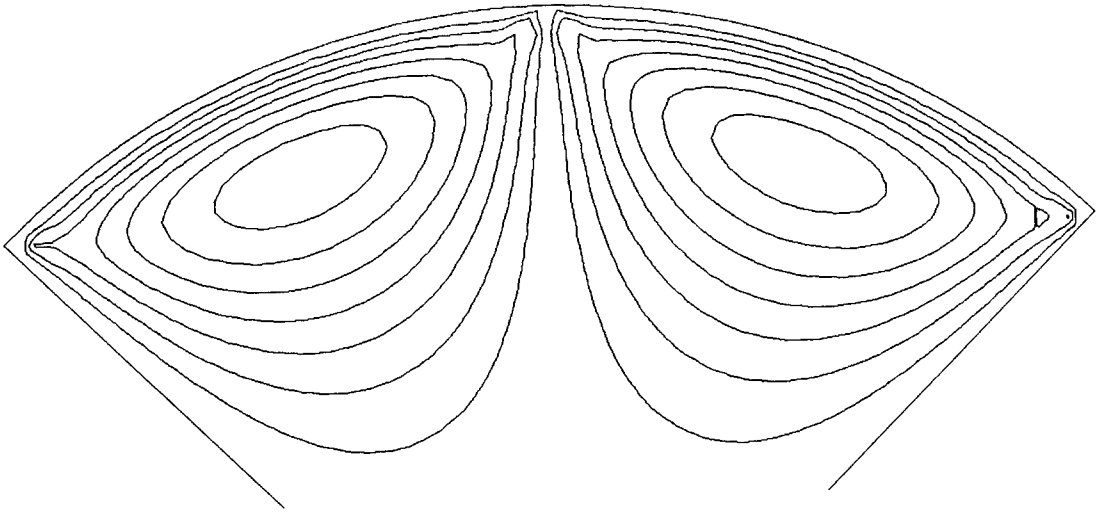

(c)

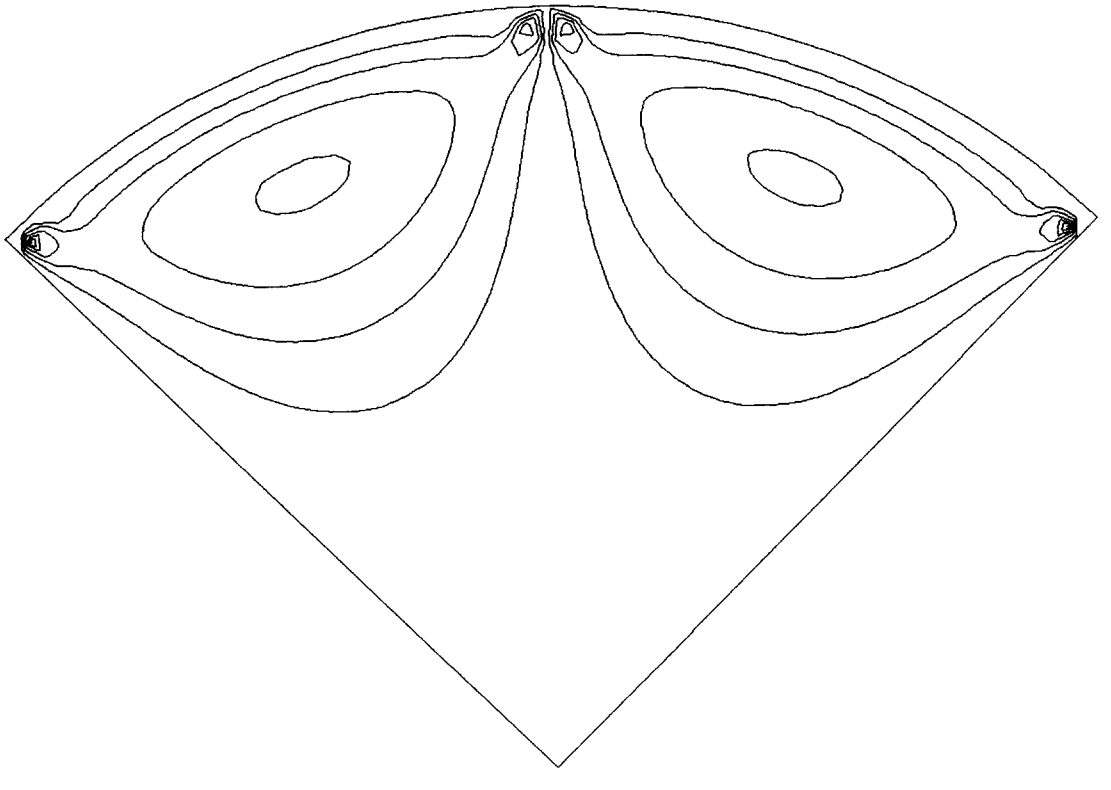

(d)

Fig. 5 (cont.).

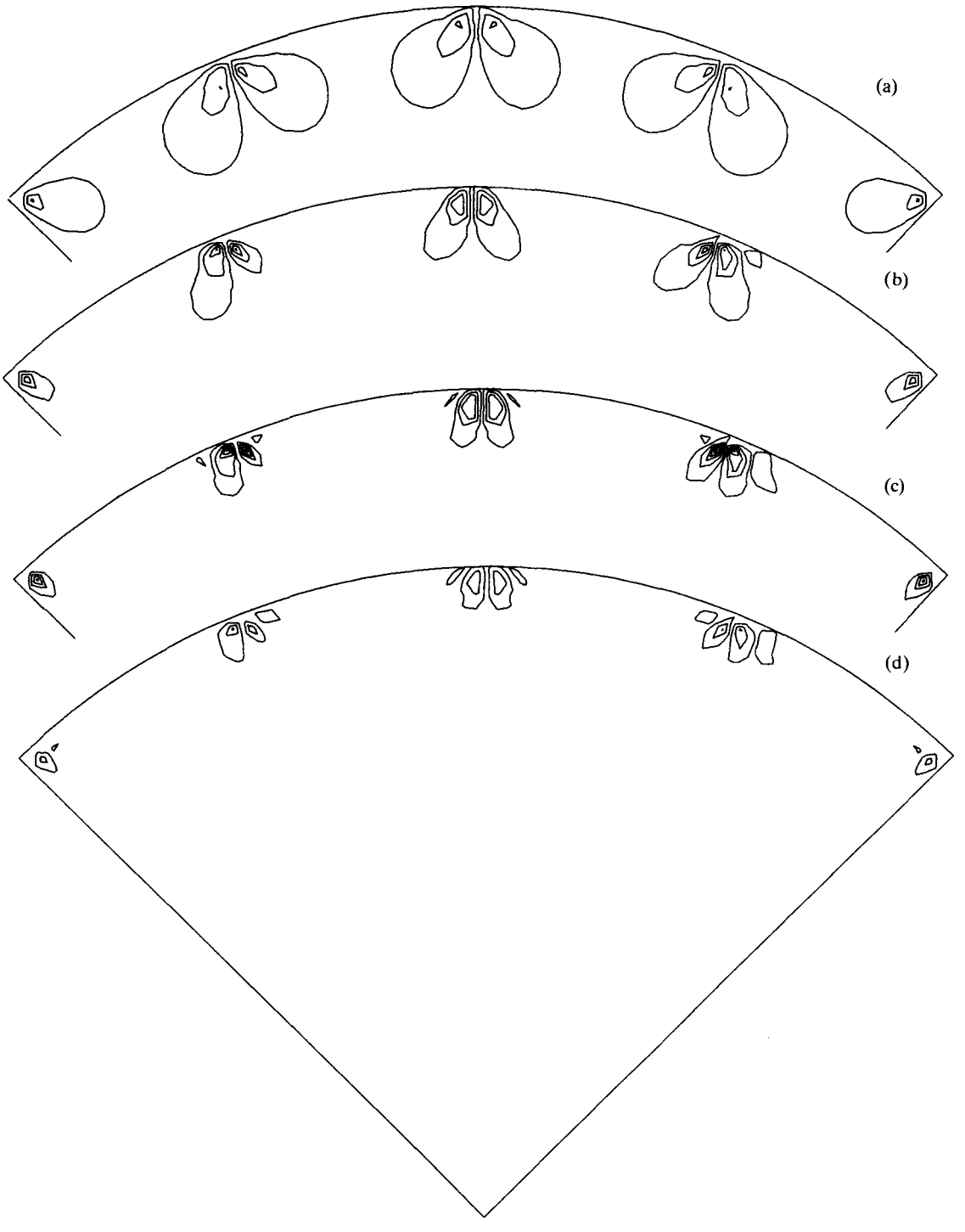

Fig. 6. As in Fig. 4, with initial concentration distribution perturbed at five locations on the interface.

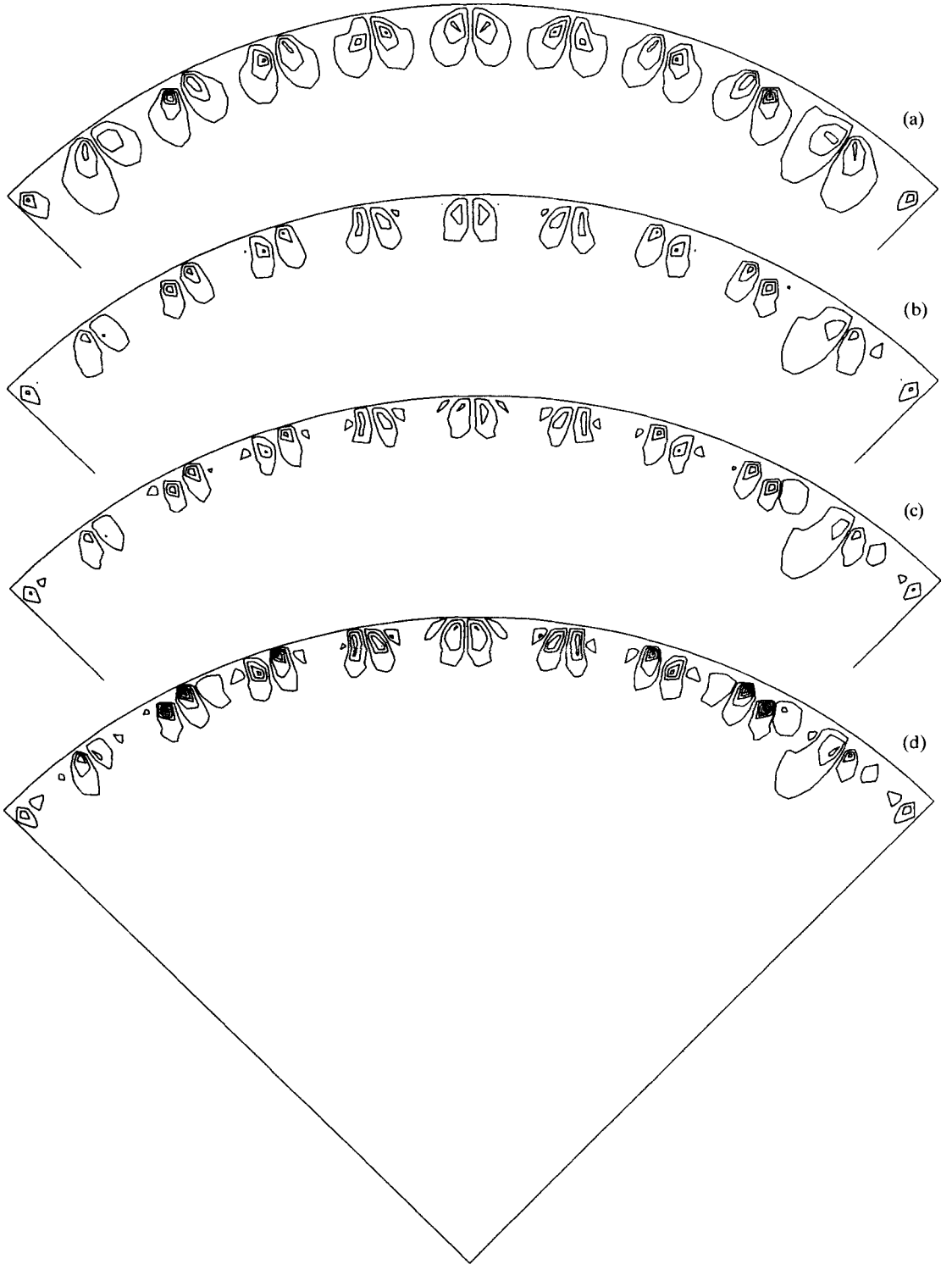

Fig. 7. As in Fig. 4, with initial concentration distribution perturbed at eleven locations on the interface.

5. Concluding remarks

The numerical results presented in this chapter confirm the experimentally observed phenomena for Marangoni convection in V-shaped containers as described by Hoefsloot et al. [7]. The triangular container (case I) shows a flow behaviour which is characteristic for macroconvection: a rather stable roll-cell pattern consisting of a small number of large cells, extending into the bulk region. The time development of the pattern is more rapid than in the case of microconvection and also the flow velocities are larger. The computations involving the circular-sector container (case II) give rise to typical microconvection behaviour: small flow velocities, slow development of flow pattern and nearly motionless liquid bulk. The initial tendency is towards breakup of cells, but after longer times it is to be expected that coalescence of cells will lead to a more or less persistent pattern of somewhat larger cells. However, an accurate and numerically stable simulation of this long-term behaviour would require the availability of a considerable amount of computing time on a very large (super)computer.

References

1. H.A. Dijkstra and A.I. van de Vooren, Initial flow development due to Marangoni convection in a mass transfer system. *Int. J. Heat Mass Transfer* 28 (1985) 2315–2322.
2. H.A. Dijkstra and J.H. Lichtenbelt, Mass transfer driven Marangoni convection under microgravity. *Appl. Microgravity Technology* 1 (1988) 180–187.
3. H.C.J. Hoefsloot and L.P.B.M. Janssen, MASER-2 report, in: *Experiment reports from flight opportunities on MASER-1 and -2 supported by ESA*, J.P.B. Vreeburg (ed.), National Aerospace Laboratory NLR, Amsterdam, The Netherlands (1989).
4. H.C.J. Hoefsloot and L.P.B.M. Janssen, Marangoni convection mass transfer, in: *Microgravity experiments during parabolic flights of KC-135 aircraft, sixth ESA campaign August 1988*, A. Gonfalone, V. Pletser and D. Frimout (eds), ESTEC, Noordwijk, The Netherlands (1989).
5. H.C.J. Hoefsloot, H.W. Hoogstraten, A. Hoven and L.P.B.M. Janssen, Marangoni instability in a liquid layer bounded by two coaxial cylinder surfaces. *Appl. Sci. Res.* 47 (1990) 1–21.
6. H.C.J. Hoefsloot, H.W. Hoogstraten and L.P.B.M. Janssen, Marangoni instability in a liquid layer confined between two concentric spherical surfaces under zero-gravity conditions. *Appl. Sci. Res.* 47 (1990) 357–377.
7. H.C.J. Hoefsloot, L.P.B.M. Janssen, R.T. Sibbald and H.W. Hoogstraten, Experimental results from Marangoni convection in V-shaped containers under microgravity conditions. *Microgravity Sci. Technology* 4 (1991) 55–59.
8. H.C.J. Hoefsloot, H.W. Hoogstraten, L.M.B.M. Janssen and J.W. Knobbe, Growth factors for Marangoni instability in a spherical liquid layer under zero-gravity conditions. *Appl. Sci. Res.* (to appear).
9. H.C.J. Hoefsloot, H.W. Hoogstraten and L.P.B.M. Janssen, Marangoni convection round a ventilated air bubble under microgravity conditions, submitted to *Chem. Engineering Sci.*
10. J.H. Lichtenbelt, Improvement of flight hardware and isothermal Marangoni convection under microgravity conditions. *Adv. Space Res.* 5 (1986) 97–100.
11. J.H. Lichtenbelt, A.A.H. Drinkenburg and H.A. Dijkstra, Marangoni convection and mass transfer from the liquid to the gas phase. *Naturwissenschaften* 73 (1986) 356–359.
12. A.D. Myshkis, V.G. Babskii, N.D. Kopachevskii, L.A. Slobozhanin and A.D. Tyuptsov, *Low-gravity Fluid Mechanics*. Springer Verlag, Berlin/New York (1987).
13. D.A. Nield, Surface tension and buoyancy effects in cellular convection. *J. Fluid Mech.* 19 (1964) 341–352.
14. R. Peyret and T.D. Taylor, *Computational Methods for Fluid Flow*. Springer Series in Computational Physics, Springer Verlag, Berlin/New York (1983).